WILEY-VCH

Embedded Fluidic Sensing and Control with Soft Open-Cell Foams

*Anoop Rajappan, Zhen Liu, Te Faye Yap, Rawand M. Rasheed, and Daniel J. Preston**

A. Rajappan, Z. Liu, T. F. Yap, R. M. Rasheed, D. J. Preston
Department of Mechanical Engineering, Rice University, 6100 Main St, Houston, TX 77005, USA
*E-mail: djp@rice.edu

Keywords: compressible flow, foam, force sensors, haptics, pneumatic logic, textile wearables

Abstract

The synthesis of soft matter intelligence with circuit-driven logic has enabled a new class of robots that perform complex tasks or conform to specialized form factors in unique ways that cannot be realized through conventional designs. Translating this hybrid approach to fluidic systems, the present work addresses the need for sheet-based circuit materials by leveraging the innate porosity of foam—a soft material—to develop pneumatic components that support digital logic, mixed-signal control, and analog force sensing in wearables and soft robots. Analytic tools and experimental techniques developed in this work serve to elucidate compressible gas flow through porous foam sheets, and to inform the design and validation of foam-enabled fluidic resistors. When embedded inside soft robots and wearables, these resistors facilitate diverse functionalities spanning both sensing and control domains, including digital logic using textile logic gates, digital-to-analog signal conversion using ladder networks, and analog force sensing via compression-induced variations in fluidic resistance. By combining features of both circuit-based and materials-based approaches, foam-enabled fluidic circuits serve as a useful paradigm for future hybrid robotic architectures that fully embody the sensing and computing capabilities of soft fluidic materials.

1. Introduction

Robots and wearables made of soft materials, such as elastomers and textiles, offer inherent advantages over their rigid counterparts in applications requiring conformability, user comfort, safety, and adaptability in interacting with humans or unstructured environments.[1–6] Through many decades of research and development, fluidic actuation and control have remained a mainstay of soft robotics, complementing or emulating electronic logic circuits and frequently outperforming electrostatic, magnetic, thermal, and chemical modes of actuation in usable force output and response time; fluidic systems by far outnumber other modes of actuation and control in contemporary soft robotic devices.[7–9] Pneumatic control systems, in particular, have evolved alongside soft robots and are now capable of complex digital and analog computations, functionally complete Boolean logic, memory storage, sequential operations, and direct interfacing with soft actuators and sensors.[10–16]

The architecture of pneumatic logic circuits in soft robots has traditionally mirrored that of electronic circuits, with discrete components such as resistors, capacitors, diodes, gates, and oscillators interconnected by fluidic lines; this conventional paradigm for designing fluidic circuits had previously been widely and successfully utilized in microfluidic devices.[11,17] Recently, however, a departure from this traditional approach has emerged, with focus shifting toward embodying computational intelligence directly within the structure of the robot or its constituent materials.[18–22] Such materials-based information processing typically exploits either the intrinsic properties of the robotic material (such as its conductivity,[23,24] magnetization,[25,26] or porosity[27]), or its engineered response to extrinsic forces (such as mechanical snap-through between bistable configurations),[28–32] to aid or effectuate logic computations. Even in robots that do not rely substantially on materials-based computing, simply leveraging the innate properties of soft materials to facilitate sensing, actuation, and control functions can itself confer many potential benefits, including (i) a simplified architecture, (ii) decentralized and distributed computing that minimizes interconnections between subsystems, (iii) tighter, materials-level integration between form and function, and (iv) fewer, more efficiently designed parts, with concomitant reduction in weight, cost, complexity, and failure points. In this "hybrid" approach to fluidic logic, robots or wearables combine features of both circuit-based and materials-based computing: conventional circuit components are redesigned to incorporate soft materials as core functional elements enabling processing and conversion of fluidic signals, and not merely as structural walls defining flow pathways and conduits. Even as such hybrid control schemes open exciting avenues for the future evolution of traditional fluidic robots toward intelligence, their continued success hinges on the development of new fluidic circuit components that substantially leverage the flow modulation, transduction, and computing capabilities of soft robotic materials.

Here, we exemplify this hybrid approach by leveraging the viscous flow of gas through a soft, porous material to create pneumatic resistance networks that enable mechano-fluidic sensing and mixed-signal control in robots and wearable devices. Specifically, we explore the use of open-cell polyurethane foam (**Figure 1**a), a soft planar material that can be easily integrated into flexible robots and body-conforming wearables, especially those built from two-dimensional materials such as textiles. Replacing serpentine channel resistors with embedded foam resistors mitigates existing design challenges and confers many practical benefits, such as ease of manufacturing, compact footprint, and resilience to mechanical deformation, in addition to well-defined, predictable, and reproducible flow characteristics. Through modeling and experiments, we systematically characterize the fluidic resistance arising from the intrinsic porosity of foam (Figure 1b), develop design rules for geometric sizing of resistors, and quantify changes in resistance under uniaxial

compressive loads. We demonstrate the capabilities of embedded foam resistors in enabling pneumatic digital logic (Figure 1c) and digital-to-analog signal conversion (Figure 1d) in textile wearables, and introduce force-sensing pneumatic resistors that output an analog pressure signal in response to applied force (Figure 1e); these varied applications illustrate the versatility of foam-enabled fluidic circuits in supporting diverse robot functionalities (sensing, control, and actuation) that span multiple (analog, digital, and mixed) signal domains, permitting economy of circuit components and the flexibility to interface directly with both digital controllers as well as analog actuators or sensors.[15]

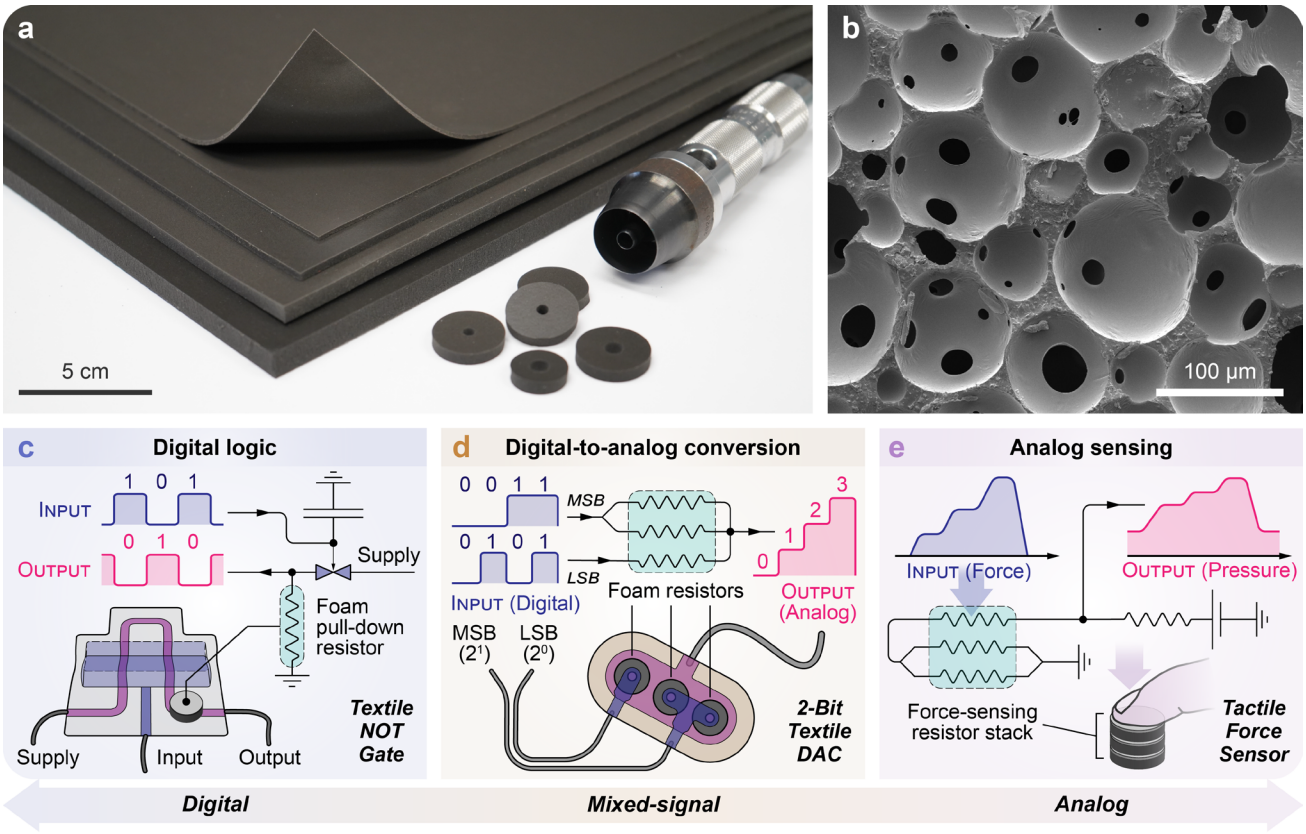

Figure 1. a) An assortment of fluidic resistors made from soft, open-cell polyurethane foam; compact annular resistors are easily manufactured from foam sheets using a hole punch. b) The internal structure of the foam consists of a dense network of interconnected pores that act as high-resistance pathways for fluid flow. c–e) Fluidic circuits built using embedded foam resistors enable digital logic, signal conversion, and analog sensing capabilities in soft robots and wearables.

2. Results

2.1. Compressible flow though porous foam sheets

To realize embedded pneumatic resistance networks, we leverage the frictional pressure drop accompanying the throttling (or isenthalpic expansion) of compressed gas through porous media, specifically thin sheets of soft, open-cell polyurethane foam. Friction arises from viscous dissipation

as the flow traverses the porous microstructure of the foam, consisting of densely packed spherical cells averaging about 100 µm in diameter, interconnected by circular pores approximately 10–30 µm in size (Figure 1b; Figure S2 and S3, Supporting Information). To ensure in-plane confinement of the flow, foam sheets of uniform thickness were heat sealed between two layers of gas-impermeable thermoplastic nylon, thus preventing leakage of gas across the top and bottom faces; these nylon layers, each approximately 50 µm thick, are visible in the cross-sectional image of the sheet resistor shown in **Figure 2**a.

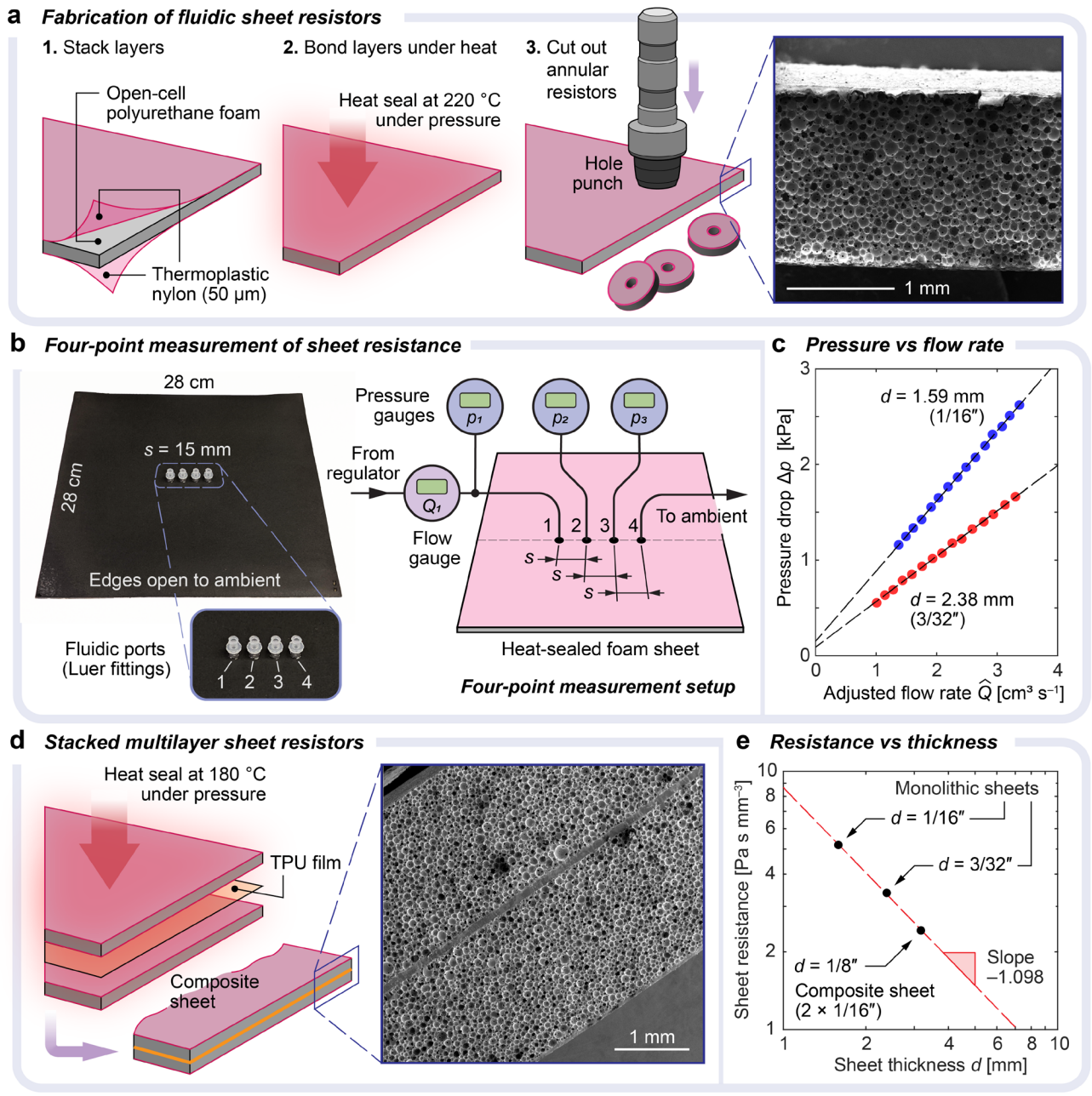

Figure 2. a) Flexible sheet resistors were made by heat-sealing open-cell polyurethane foam between two layers of gas-impermeable thermoplastic nylon. Annular resistors of the required sizes were cut from these sheets and used to build fluidic circuits. b) We developed a fluidic analog of the four-

point probe method to characterize the resistance to air flow through heat-sealed foam sheets. c) Experimentally measured pressure drop $\Delta p = p_2 - p_3$ as a function of the air flow rate $\hat{Q}$ for sheet resistors of two different thicknesses. The slopes of the best-fit lines from three such measurements were averaged to determine the sheet resistance of each foam sheet. d) Where monolithic sheets of the required thickness were unavailable, composite sheet resistors were assembled by stacking and bonding multiple sheet resistors using heat-sealable thermoplastic polyurethane (TPU). e) The experimentally measured sheet resistance R_S varies inversely as the thickness d for both monolithic and composite sheets, consistent with Equation 3.

Over the usual range of operating pressures (1–5 bar) encountered in our foam-enabled pneumatic circuits, compressed air obeys the ideal gas law and exhibits minimal Joule-Thomson cooling on expansion; furthermore, at typical flow rates, effects of flow inertia on the dynamics of permeation remain small and may be neglected during analysis (Section S1, Supporting Information). Under these conditions, we show that the steady, compressible, two-dimensional flow field inside the porous sheet is prescribed uniquely by the requirement that the square of the absolute gas pressure p solves Laplace's equation:

$$\nabla^2 p^2 = 0 \tag{1}$$

For arbitrary flow domains, solutions for the spatially varying pressure field $p(x, y)$ inside the sheet may thus be obtained by superposing harmonic functions with suitable boundary conditions enforced at the edges. Gas flow within the foam sheet is related to the pressure gradient by Darcy's law,[33]

$$\boldsymbol{\nabla} p = -R_S \, \boldsymbol{q} \tag{2}$$

where $\boldsymbol{q} = d \, \boldsymbol{u}$ is the two-dimensional gas flux parallel to the plane of the sheet, $\boldsymbol{u}$ is the superficial gas velocity, and the constant of proportionality

$$R_S \coloneqq \frac{\mu}{Kd} \tag{3}$$

defines a material parameter that combines spatially invariant properties of both the fluid (dynamic viscosity μ) and the foam (sheet thickness d and permeability K). We term R_S the "(fluidic) sheet resistance" insofar as it quantifies the two-dimensional pneumatic resistance of a porous foam layer of a given thickness; its role in Equation 2 is analogous to that of the electrical sheet resistance ρ_S in Ohm's law, $\boldsymbol{i} = -\rho_S \, \boldsymbol{\nabla} V$, relating the current density $\boldsymbol{i}$ in a planar conductor to the potential gradient $\boldsymbol{\nabla} V$. Exploiting this analogy between current flow in thin films and gas flow through porous sheets, we developed a fluidic version of the electrical four-point probe method commonly used to measure the sheet resistance of conductive films and coatings (Figure 2b).[34,35] Our "fluidic four-point probe" consisted of four equally spaced pneumatic ports connected to pressure and flow rate sensors,

mirroring the paired voltage and current sensing contacts, respectively, present on the electrical probe. To characterize the fluidic resistance of the foam, we measured the pressure difference $\Delta p = p_2 - p_3$ across the inner pair of ports as a function of the known flow rate of gas, Q_1, entering the inlet port (Figure 2c). The sheet resistance R_S was then inferred from the slope of the pressure vs flow rate curve according to

$$R_S = \beta \frac{\pi}{\ln 2} \frac{\Delta p}{\hat{Q}} \tag{4}$$

where $\hat{Q} = Q_1 \cdot 2p_1/(p_2 + p_3)$ is the "adjusted" flow rate that accounts for the expansion of gas as it flows through the foam, and β is a geometric coefficient that corrects for the finite extent of the sheet and the attendant edge effects on the flow field (Section S3, Supporting Information). The scale invariance of the governing equation (Equation 2) suggests that the geometric coefficient β is a function only of the size a and spacing s of the fluidic ports relative to the lateral dimension L of the test specimen, i.e., $\beta = \beta(a/s, s/L)$; its precise value was derived from a finite element analysis of the flow field for our specific test geometry (Section S3 and Figure S1b, Supporting Information).

In Figure 2c, we show the experimentally measured flow curves for two different sheet resistors, made from monolithic foam sheets of identical porosity but different thicknesses. Additionally, we tested composite sheet resistors (Figure 2d) for which the desired thickness was built up by stacking multiple sheets that were then thermally bonded together using heat-sealable films of thermoplastic polyurethane (TPU). Regardless of the fabrication process, monolithic and composite sheets alike yielded fluidic sheet resistances that varied inversely proportional to their thickness, $R_S \sim d^{-1}$, in accordance with Equation 3 (Figure 2e). Besides the design flexibility afforded by the ability to realize a range of fluidic resistances by combining sheets from a finite set of readily available thicknesses, the data in Figure 2e also confirms that the loss of flow cross-section, if any, due to "skin effects" at the heat-sealed boundaries of the foam sheet is minimal and may be safely neglected in resistance computations.

2.2. Annular resistors

To fashion the individual resistors needed to assemble our embedded fluidic circuits, we used a concentric hole punch (Figure 1a) to cut circular rings (annuli) from sheet resistors of the requisite thickness. Each annular resistor, as shown in **Figure 3**a, is characterized by its in-plane dimensions (inner radius r_1 and outer radius r_2), as well as the thickness d (or equivalently, the sheet resistance R_S) of the foam sheet from which it was made. To study the resistor's flow characteristics, we configured fluidic connections such that pressurized gas is fed through an inlet port to the center of

the annulus, flows radially outward through the body of the resistor, and exits at atmospheric pressure via the outer edge. For steady radial flow inside a concentric annulus, solving Equation 1 in cylindrical coordinates yields the theoretical pressure profile

$$p^2(r) = p_2^2 + (p_1^2 - p_2^2)\frac{\ln(r/r_2)}{\ln(r_1/r_2)} \tag{5}$$

where p_1 and p_2 are, respectively, the absolute gas pressures at the inner and outer edges of the resistor, and r denotes the radial distance measured from the center of the annulus (Section S4, Supporting Information). We define the fluidic resistance R for pneumatic resistors by analogy with the ohmic resistance of electronic resistors, and show (by combining Equation 5 and 2) that its theoretical value for an annular resistor is given by:

$$R \coloneqq \frac{\Delta p}{\hat{Q}} = \frac{R_S}{2\pi}\ln\left(\frac{r_2}{r_1}\right) \tag{6}$$

Here, Δp is the pressure drop across the resistor, $\hat{Q} = 2p_1Q_1/(p_1 + p_2) = 2p_2Q_2/(p_1 + p_2)$ is an adjusted flow rate that accounts for the expansion of the gas, and R_S is the sheet resistance of the body of the resistor as determined from four-point probe measurements on the parent foam sheet. We note that the resistance is a function only of the geometric aspect ratio r_2/r_1, and is independent of both the direction of flow (radially inward or outward) and the actual resistor dimensions; indeed, these properties hold generally for resistors of arbitrary shape (including annular resistors), and follow directly from the linearity of Equation 3 and its invariance under isometric scaling.

Figure 3b shows a few representative examples of flow curves measured experimentally for annular resistors of varying dimensions—in this case, resistors with the same inner radius but of differing outer radii. The pressure drop vs flow rate relationships are linear, in conformance with Equation 6, corroborating our assertion that the effects of flow inertia are negligible. We compared the fluidic resistance R inferred from the slope of these lines against the theoretical resistance predicted by Equation 6, and found good agreement across varying radial dimensions and sheet thicknesses (Figure 3c). Furthermore, as in the case of sheet resistors, the experimentally measured resistances of multilayer resistors agreed well with the theoretical values calculated based on the aggregate thickness of the composite sheet (Figure 3d).

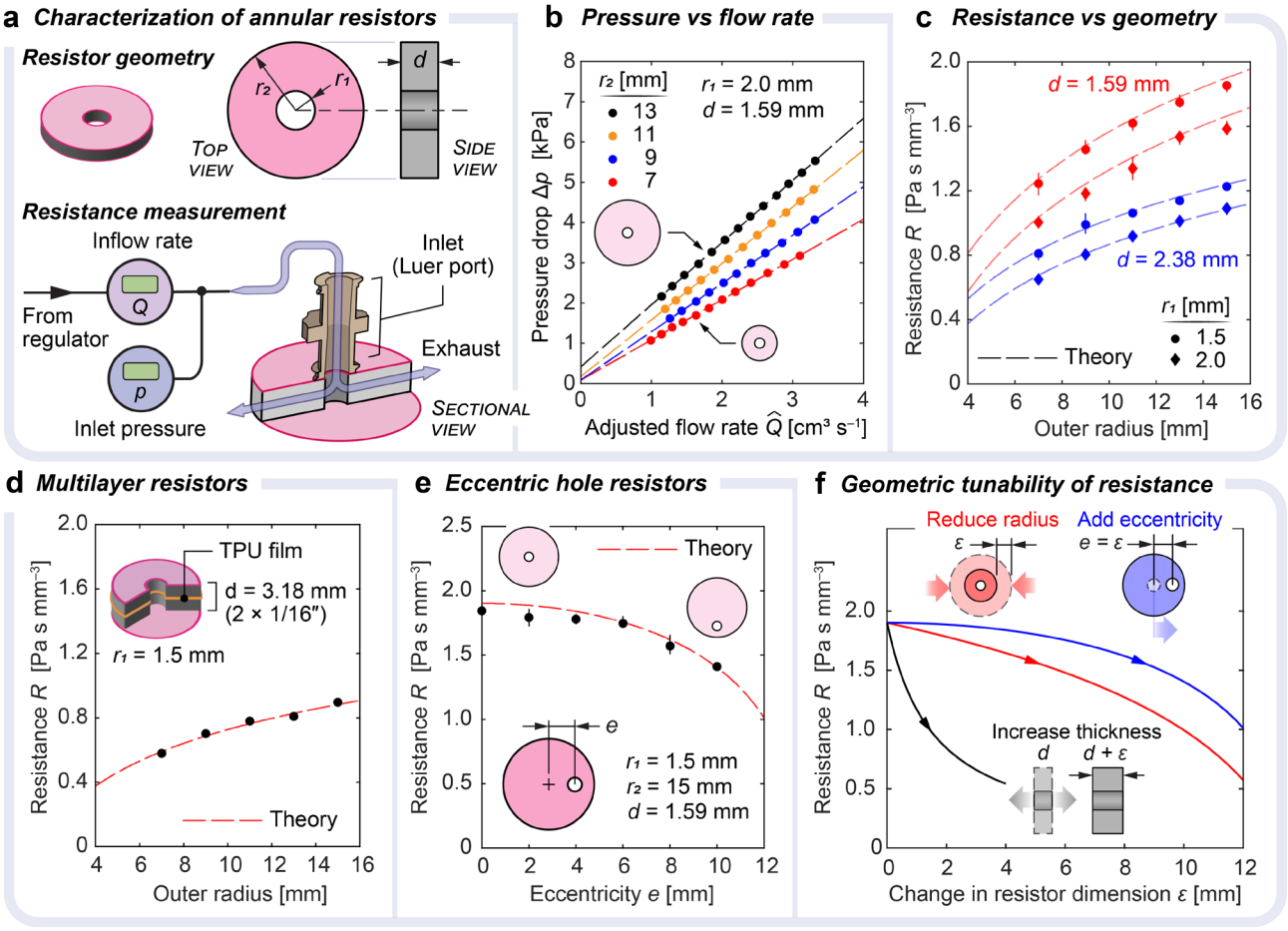

Figure 3. a) Annular geometry of foam-enabled pneumatic resistors. To characterize the fluidic resistance, we measured the flow rate of air as a function of the inlet pressure. b) Representative measurements of the pressure drop as a function of flow rate for annular resistors of different dimensions. The flow curves are linear, and the slope of the best fit line quantifies the fluidic resistance. c–e) Experimentally measured resistances show good agreement with theory for c) annular resistors of different radial dimensions and sheet thicknesses, d) multilayer resistors made from composite sheets, and e) resistors of varying hole eccentricities. Data points in c) and e) denote measurements averaged over three resistors, and those in d) were averaged over two resistors. f) For the same change in dimension ε, the resistance R is most sensitive to changes in sheet thickness ($d' = d + \varepsilon$), moderately sensitive to changes in the radius ($r_2' = r_2 - \varepsilon$), and least sensitive to changes in eccentricity ($e = \varepsilon$). The initial dimensions of the resistor are r_1 = 1.5 mm, r_2 = 15 mm, d = 1.59 mm, and e = 0 mm.

In addition to the concentric annular geometry discussed above, we investigated the flow through "eccentric" annuli for which the interior hole is displaced radially by a distance e ($0 < e < r_2 - r_1$). To analyze this flow, we transformed the governing equations into bipolar coordinates (Section S5, Supporting Information) and solved them to obtain the theoretical resistance of a porous annulus of eccentricity e:

$$R = \frac{R_S}{2\pi}\cosh^{-1}\frac{1}{2}\left(\frac{r_1}{r_2}+\frac{r_2}{r_1}-\frac{e^2}{r_1 r_2}\right) \quad (7)$$

This expression compares well with our experimental measurements for a sequence of resistors with increasing eccentricity, as shown in Figure 3e. The provision of a non-zero eccentricity e augments the available design space with a third independent dimension—besides the radius r_2 and thickness d—enabling the fine tuning of individual foam resistors for use in pneumatic circuits. To illustrate the varying degrees of geometric tunability afforded by changing each of the three parameters, we consider a typical resistor (of initial dimensions r_1 = 1.5 mm, r_2 = 15 mm, d = 1.59 mm, and e = 0 mm) and compare the change in resistance R caused by identical changes (of size ε) to either the thickness d, the radius r_2, or the eccentricity e (Figure 3f). Of the three cases, the resistance R is the most sensitive to changes in sheet thickness, $R \sim d^{-1}$, and moderately sensitive to changes in the radius, $R \sim \ln r$. By contrast, introducing a small non-zero eccentricity elicits only a gradual change in R, permitting fine adjustments to be made to the overall fluidic resistance. In fact, for small deviations $e = \varepsilon$ from concentricity, Equation 7 implies that the resistance is unchanged to the first order in ε, i.e., $\Delta R = 0 + \mathcal{O}(\varepsilon^2)$. Thus, when optimizing resistors for mass production, small errors in locating the central hole do not incur significant inaccuracies in resistance, permitting more forgiving manufacturing tolerances for punches and dies used to stamp resistors from sheet stock.

2.3. Foam-enabled pull-down resistors for digital logic

Owing to their soft structure, compact size, and planar, low-profile form factor, foam-enabled fluidic components are well-suited for use in embedded logic circuits in wearables, especially those built from sheet-based materials such as textiles. We previously developed a textile-based digital logic architecture that enabled Boolean logic computations, user interaction, memory storage, and actuator control in wearable robots entirely via textile-embedded pneumatic circuits.[14] Besides the immediate advantages of user comfort and the ability to integrate fluidic circuits seamlessly into clothing, the construction of logic components from durable fabric materials confers additional benefits such as washability, mass manufacturability using existing textile processes, and resistance to damage and wear incurred in daily use.[14] In this context, the two-dimensional geometry of our foam-enabled pneumatic resistors lends itself excellently to embedment between layers of thermoplastic-coated fabric, enabling mass production of logic-capable textile laminates and wearables via batch or continuous heat sealing operations.

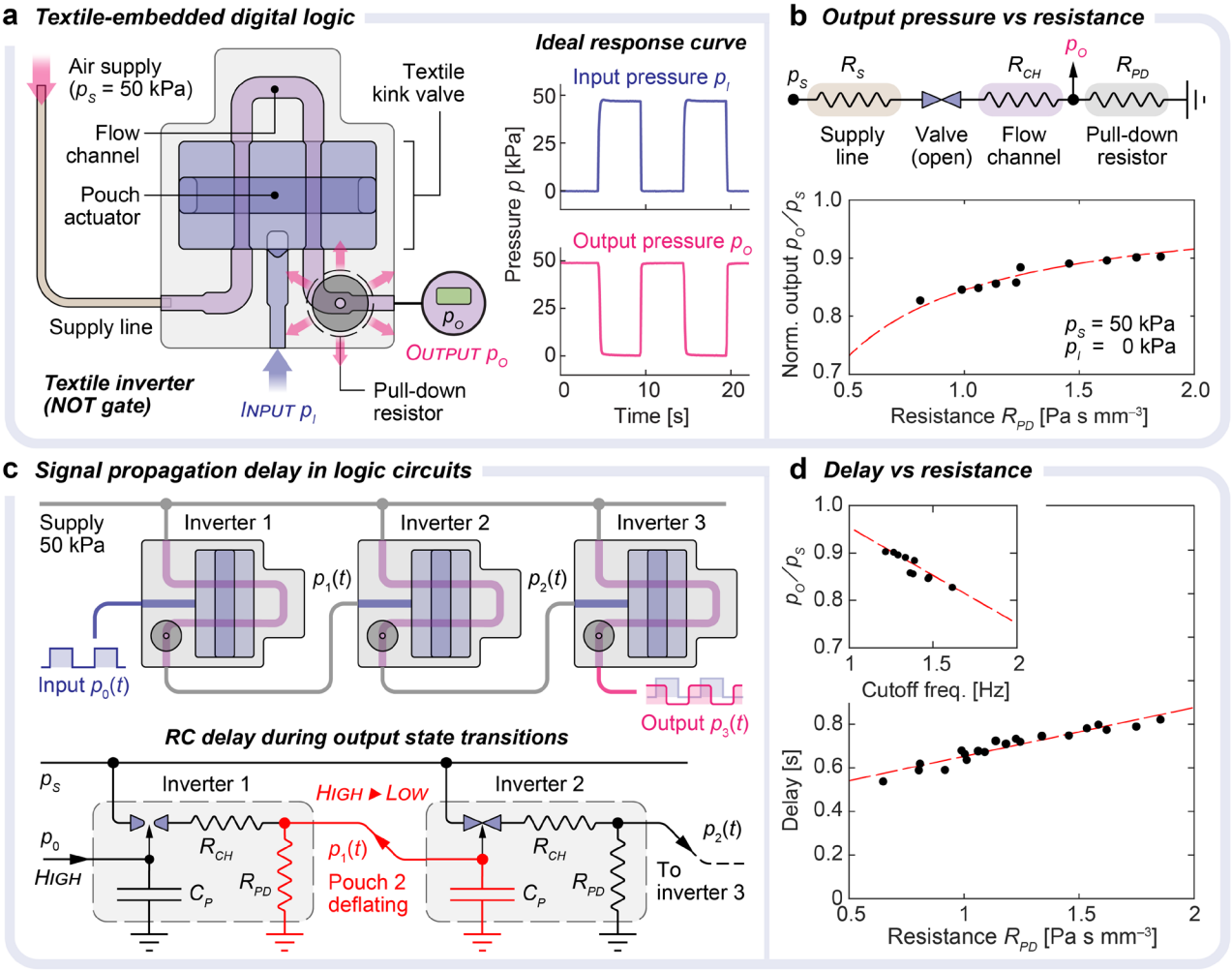

Figure 4. a) The internal layout of the textile inverter. A foam-enabled pull-down resistor is attached to the output line. b) The normalized output p_O/p_S of the inverter in the "on" (high output) state drops with decreasing pull-down resistance R_{PD}; the dashed curve denotes the predicted output for a total upstream resistance of $R_S + R_{CH}$ = 0.22 Pa s mm^{-3}. Data were averaged over three replicate measurements. c) We characterized the speed of our logic circuits by measuring the propagation delay across a network of three inverters. The schematic diagram in the bottom half explains the origin of the RC delay during output signal transitions from high to low. d) The time delay Δt per inverter stage (averaged over both rising and falling signal transitions) increases with increasing pull-down resistance R_{PD}. The inset shows the tradeoff between the output signal strength p_O/p_S and the cutoff frequency $f = 1/\Delta t$. Dashed lines are included only for visual guidance.

The foundational component of our textile-based logic architecture is the textile inverter,[14] shown schematically in **Figure 4**a; briefly, it consists of paired pouch actuators linked pneumatically to the input port, overlying an embedded flow channel that connects the supply port to the output port. When the digital input to the inverter is "low" (input pressure $p_I \simeq 0$ kPa gauge), the pouches are deflated and the channel is open, permitting unobstructed flow of pressurized gas (at p_S = 50 kPa gauge) from the supply port to the output. When the input is switched to "high" ($p_I \simeq p_S$), the pouches inflate and produce folds (or kinks) in the flow channel, preventing flow from the supply

line to the output port. Such a device comprising a flexible channel embedded between inflatable pouches (and assembled entirely from stacked and heat-sealed textile layers) thus behaves as a soft pneumatic switch or relay. To convert this fluidic relay to a full-fledged digital inverter (i.e., a NOT gate), we add a fluidic pull-down resistor to the output line, mirroring the construction of electronic inverters from transistors in resistor-transistor logic circuits;[36] the resistor provides an exhaust pathway for air downstream of the kink, depressurizing the output line and thus driving the signal low when the input to the inverter is high. Equipped in this fashion with a foam-enabled pull-down resistor, the textile inverter converts a high-pressure input signal (a digital "1") to a low-pressure output signal (a digital "0") and vice-versa (Figure 4a), yielding an elementary logic unit that may then be combined in series and parallel configurations to build networks of functionally complete digital gates capable of executing both combinational and sequential logic functions.

As in the case of electronic resistor-transistor circuits, the sizing of pull-down resistors in fluidic logic circuits entails a design tradeoff between switching speed and energy efficiency: a strong pull down (i.e., a small resistance) facilitates quick transitions of the output signal from high to low, enabling faster response times, whereas a weak pull down (large resistance) minimizes loss of compressed gas when the output is high, prolonging the life of portable devices and untethered robots that carry an exhaustible supply of pressurized gas onboard. In Figure 4b, we examine the leakage flow through the inverter in the "on" (i.e., high output) state and its influence on the output pressure level p_O. A smaller pull-down resistance R_{PD} incurs a greater outflow of gas which, in turn, manifests as a drop in the output signal strength p_O/p_S, particularly in circuits with substantial fluidic resistance in the upstream supply. The pull-down resistor must therefore be sized appropriately such that the signal level in the high output state does not fall below the minimum pressure threshold required to activate components in subsequent levels of the logic cascade.

A strong pull down, despite the leakage incurred, may however be advantageous when designing circuits that require low latency and fast response to user or sensor inputs; by enabling a faster slew rate of the output signal, a small pull-down resistance minimizes gate delay and permits circuit operation at higher frequencies. To study the influence of resistor sizing on the speed of our textile-embedded logic circuits, we measured the propagation delay of signal transitions across a network of three identical inverters connected in series, representing a simple multistage logic cascade (Figure 4c). Analogous to the case of electronic transistor-based switches, the delay in our fluidic circuits fundamentally originates from the resistive-capacitive (RC) delay inherent in the discharging (depressurization) of capacitive circuit elements, such as pouches, actuators, and fluidic interconnections. As an example, Figure 4c illustrates the scenario when the first inverter in the

cascade switches off in response to a high-pressure input signal; the subsequent transition of its output from high to low entails the depressurization, via the pull-down resistor, of the pouch actuators of the inverter in the following stage, incurring a time delay $\tau \simeq R_{PD}C_P$ where C_P is the fluidic capacitance of the pouch. In Figure 4d, we characterize the average delay per inverter, Δt, in the three-stage circuit, which grows with increasing pull-down resistance R_{PD}. The inset to the figure elucidates the tradeoff between signal strength and speed inherent in sizing annular resistors for fluidic logic; the designer may opt for faster speeds (indicated by a higher cutoff frequency $f = 1/\Delta t$) at the expense of output pressure or vice-versa, consistent with the specific needs and performance requirements of the device in question.

2.4. Digital-to-analog signal conversion

Despite the widespread transition of logic control systems from the analog to the digital domain in modern times, specialized analog circuits continue to provide unique advantages in simplifying device architecture and minimizing the number of discrete components in both electronic and fluidic systems. In soft robots, the strategic use of analog circuits has facilitated substantial reductions in the number of digital switches or logic gates required to execute complex actuation and control operations,[15] enabling onboard controllers that can operate within the strict space, weight, and power constraints of untethered robots. Mixed-signal fluidic controllers—which leverage the strengths of both analog and digital systems—thus remain a promising avenue of exploration in the effort towards building autonomous soft robots.

Digital-to-analog converters (DACs) provide a vital link between digital and analog subsystems in robots that incorporate mixed-signal fluidics to achieve sensing, actuation, and logic functions. Importantly, DACs enable digital controllers to interface with fluidic actuators commonly found in soft wearables and assistive devices—pneumatic muscles, pouch motors, inflatable bellows, and haptic sleeves—all of which operate on pressurized gas and permit graded actuation in response to continuous variation of the input pressure. To this end, we leveraged foam-enabled fluidic components to develop a soft pneumatic DAC that converts a two-bit binary input (i.e., 00, 01, 10, or 11) to a stepped, four-level analog output (**Figure 5**a); the output levels correspond to equally spaced divisions ranging from zero to the full-scale value of the analog signal. Internally, our DAC consists of three identical annular resistors arranged in a 2-bit binary-weighted network:[37] two resistors in parallel connect to the signal line carrying the most significant bit (MSB, or the 2^1 digit) of the binary input, and a single resistor connects to the line carrying the least significant bit (LSB, or the 2^0 digit) of the binary input. All three resistors, in turn, exhaust into a common plenum that is pneumatically linked to the output line. We note that the ladder architecture of our DAC, which

requires $(2^N - 1)$ identical resistors, may be readily extended to accommodate longer bit widths N for realizing a finer resolution (step size) of the output signal. The annular foam resistors that constitute the DAC were embedded between heat-sealed layers of nylon fabric to form a flexible, compact, and rugged assembly that can be easily integrated into textile devices.

Our pneumatic DAC may be configured to provide either an analog pressure or a flow rate as the fluidic output (Figure 5a), akin to electronic ladder networks that may be operated either in the voltage or the current mode.[37] Digital pressure signals were generated using a pair of manual toggle valves, with "1" (high) and "0" (low) states corresponding to supply (p_s) and atmospheric pressures, respectively. Figure 5b shows the linear regulation of flow rate, and the near-linear regulation of output pressure, achieved by the 2-bit DAC in response to binary inputs. We tested two versions of our device, identical in design except a difference in the fluidic resistance R of their respective internal resistors, which were made from foam sheets of different thicknesses d. As expected from a fluidic analysis of the ladder circuit (Section S6, Supporting Information), the sizing of internal resistors (provided they are equal) has no influence on the output levels of the DAC when operating in the pressure mode; by contrast, the output of the DAC in the flow rate mode, at a given supply pressure, is a function of both the resistance R of its internal resistors and the fluidic resistance R_O of the downstream circuit.

As an example of the fluidic control capabilities enabled by the DAC, we used a 2-bit digital input signal to regulate heat loss from a convectively cooled surface, by modulating the flow rate of an air jet striking the surface from a fixed stand-off distance (Figure 5c). The experimentally measured drop in surface temperature, and the associated heat transfer coefficient h (quantified by the Nusselt number $\mathrm{Nu} = hD/k$, where D and k are the nozzle diameter and the thermal conductivity of air, respectively), closely follow our predictions based on empirical correlations for jet impingement cooling reported in the literature[38] (Section S7, Supporting Information). A visual demonstration of the analog flow control provided by the DAC is shown in Figure 5d: successive binary inputs (at constant supply pressure) generate increasing flow rate (and exit velocity) of the jet, evidenced by the sequential quenching of candle flames positioned at progressively larger distances from the nozzle exit.

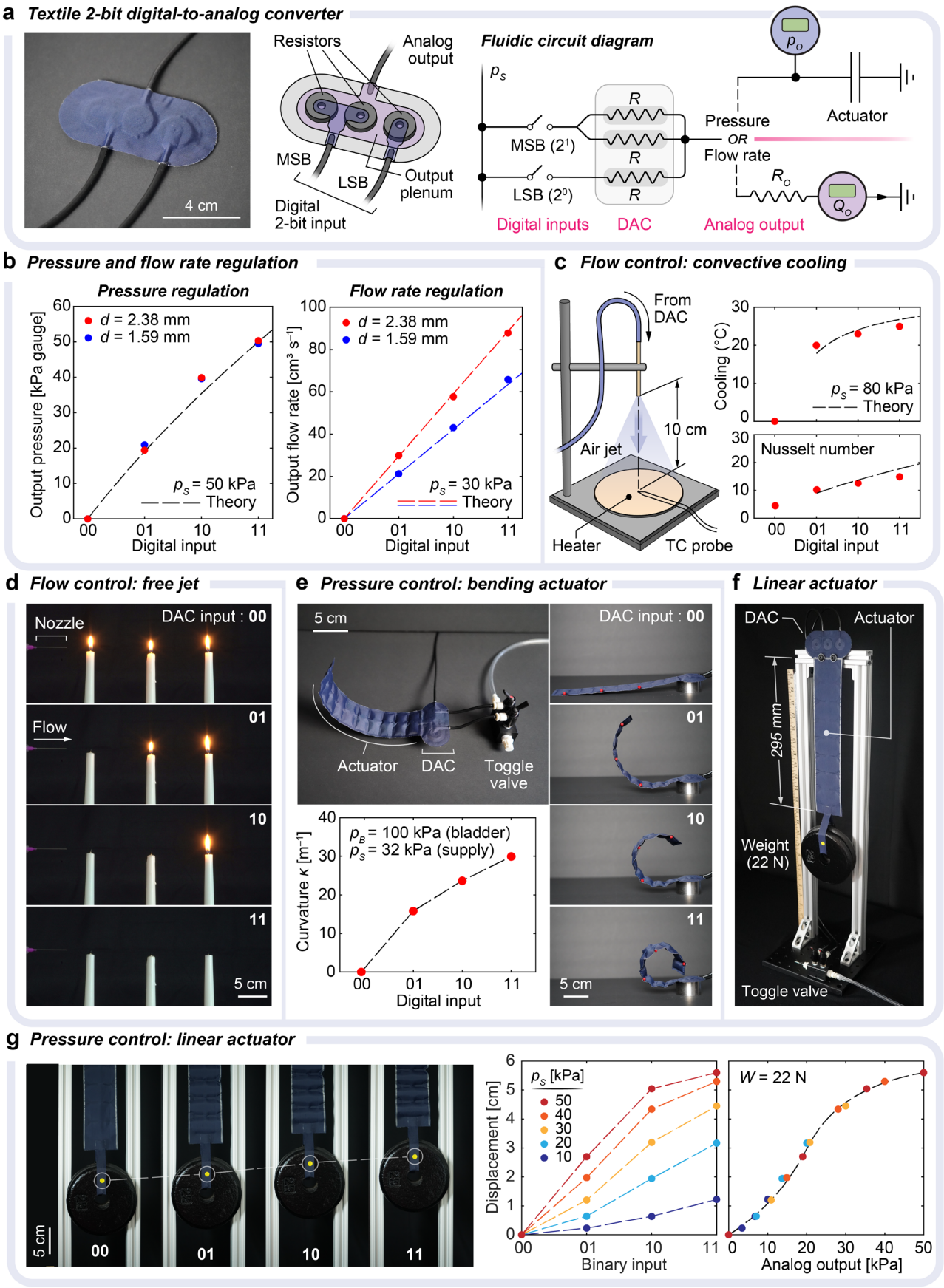

Figure 5. a) Internal layout of the 2-bit foam-enabled DAC. The circuit diagram on the right shows

the downstream configurations for operating the DAC in the pressure and flow rate modes. b) The analog pressure and flow rate output of two DACs built using resistors of different sheet thickness d. The output pressures for the two devices are identical whereas the flow rate depends on the internal resistance R. c) We routed the flow output from the DAC via a nozzle to provide jet impingement cooling of an electrically heated surface. The drop in surface temperature and the Nusselt number (dimensionless heat transfer coefficient) increase with successive binary inputs to the device. d) A visual demonstration of flow rate modulation effected by the DAC: jets of increasing strength extinguish lighted candles placed at progressively larger distances from the nozzle. e) The curvature of textile bending actuator controlled using digital pressure signals sent to its integral 2-bit DAC. f) A textile linear actuator (pouch motor array) with an integral 2-bit DAC with a weight hung from its lower end. g) The displacement of the actuator measured for different binary input signals and supply pressures. When re-plotted as a function of the output pressure of the DAC, the displacement curves measured at different pressures collapse into a single response curve for the pouch array.

The sheet-based construction of our foam-enabled DAC permits its seamless and straightforward integration into a variety of actuators and wearables built using stacked laminate assembly of heat-sealable textile layers. In Figure 5e–g, we show two such instances of textile-based pneumatic devices, wherein digital control of inherently analog actuators is facilitated by internally embedded DACs. Figure 5e shows a textile bending actuator equipped with an internal 2-bit DAC, enabling stepped control of its internal working pressure—and thereby its curvature—by means of digital signals transmitted directly to the device (Movie S1, Supporting Information). Figure 5f shows a textile linear actuator consisting of multiple gusseted pouch motors linked in series and driven by the analog output of an embedded 2-bit DAC. Digital pressure signals, generated by a set of manual toggle valves connected to the supply manifold, enable graded actuation of the pouch motors whose cumulative contraction, in turn, lifts a 22 N (5 lbf) pendent weight through varying heights (Movie S2, Supporting Information). In Figure 5g, we show the measured displacement (i.e., linear contraction) of the actuator under constant loading for different binary inputs and supply pressures; upon re-plotting the displacement against the theoretically predicted output pressure of the DAC, the individual curves for different supply pressures collapse onto a single pressure vs displacement curve that governs the underlying analog response of the pouch array.

2.5. Analog force sensing using foam resistors

The foregoing applications of foam-enabled fluidics (in digital logic and signal conversion circuits) entailed the passive utilization of a specific intrinsic property of a soft robotic material, i.e., the inherent porosity of open-cell foam. The structural intelligence inherent in soft materials, including foam, enables us to devise dynamic computing schemes that exploit not just their passive properties, but also their active response to external stimuli. In the specific case of soft, open-cell foam, we sought to leverage the microstructural changes to porosity under uniaxial compression to accomplish

fluidic sensing and transduction of the applied external force.

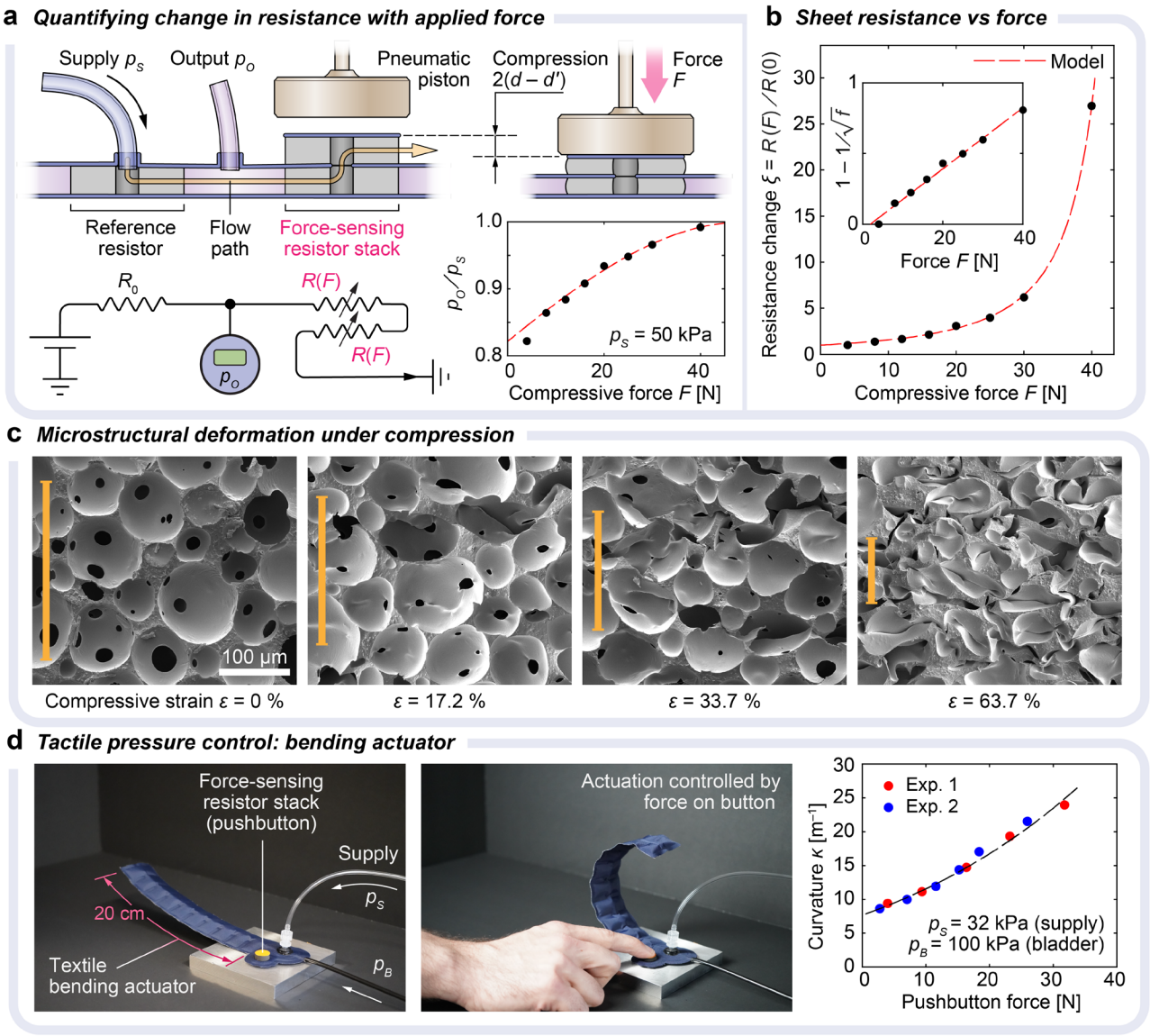

Figure 6. a) A schematic illustration of a foam-enabled force sensor built from stacked annular resistors. The analog pressure output p_O of the fluidic "voltage divider" increases with increasing magnitude of the applied force F. b) The fractional change f in the sensor's fluidic resistance is consistent with our model describing the change in sheet resistance with compression. The inset replots the data using linearly dependent variables, further validating its conformance to our proposed functional form (Equation 10). c) Progressive collapse of the cellular microstructure of foam under increasing compressive strain; images are oriented such that the axis of compression is vertical. The yellow bar depicts the affine contraction of a 250-μm long material element under the applied strain. d) The force sensor, when integrated into a textile bending actuator in the form of a pushbutton, enables analog control of the curvature based on tactile inputs from a human user. The output of the force sensing circuit drives an array of rotational pouch motors in the actuator, acting against the stiffness imparted by an integrated support bladder kept pressurized at p_B = 100 kPa.

To enable analog sensing of compressive forces, we devised a fluidic force sensor consisting of two

annular resistors of equal radial dimensions, superposed to form a concentric stack (**Figure 6**a); the resistors were permanently affixed in this configuration by heat-sealing them between layers of TPU-coated nylon. This vertically stacked arrangement ensured that (i) forces applied to the stack generated equal compressive stresses in both resistors; (ii) the resistors remained fluidically coupled in series via their coincident central holes; and (iii) flow entered and exited the stack through the periphery of the bottom and top resistors, eliminating the need for textile channels or fluidic connections to be routed to the center of the annulus where they might be constricted by the applied external force. We placed the force-sensing resistor stack in series with a reference resistor R_0 supplied by a known upstream pressure p_S, creating a fluidic "voltage divider" analogous to those commonly used with electronic force-sensing resistors. Variations in the fluidic resistance of the stack in response to compressive strain yielded an analog pressure signal p_O that we correlated with the magnitude of the applied external force F (Figure 6a).

In contrast to electronic force-sensing resistors that typically exhibit a decrease in resistance with increasing force, the fluidic resistance of open-cell foam sheets increases with increasing compressive strain normal to the plane of the sheet. This increase in flow resistance can be attributed to two concurrent effects: the permeability of foam decreases as internal cells deform and buckle under compression, reducing their effective porosity; at the same time, the thickness of the sheet is reduced, causing a diminution in the cross-sectional area available to the flow. To quantify the fluidic response of our foam sheets to compressive strains, we measured the output pressure $p_O(F)$ from the divider circuit for known amounts of the force F exerted on the stack by means of a pressure-regulated pneumatic cylinder; the corresponding fractional change in the resistance of the stack was then inferred from the expression

$$\xi \coloneqq \frac{R(F)}{R(0)} = \frac{R_o}{2R(0)} \cdot \frac{p_O^2 - p_\infty^2}{p_S^2 - p_O^2} \tag{8}$$

where $R(0)$ and $R(F)$ are, respectively, the fluidic resistances of the stacked annular resistors in the undeformed and compressed states, and p_∞ is the exhaust pressure of gas at the outlet of the stack. Guided by existing models for the change in permeability of open-cell foams with compression,[39,40] we derived a mechanistically founded functional form that describes the non-linear dependence of the normalized resistance ξ on the applied force (Section S8, Supporting Information):

$$\xi = \frac{1}{(1 - \eta F)^2} \tag{9}$$

The material response in our model is thus fully characterized by a single free parameter, η, which

quantifies the compliance of the foam under uniaxial compressive loads. As evidenced by the curve fit in Figure 6b, our proposed model shows excellent agreement with experimental measurements, with least-squares regression yielding η = 0.020 N^{-1} for our foam sheets. To reaffirm the validity of the fit to Equation 9, we rearranged its terms to obtain an equivalent linear formulation given by

$$1 - \frac{1}{\sqrt{\xi}} = \eta F \tag{10}$$

which directly yields the parameter η as the slope of the best-fit line. The inset to Figure 6b confirms that the experimental data, replotted in these new variables, conforms to a straight line with its slope consistent with the value of η obtained from the original fit.

The sequence of images in Figure 6c reveals the microstructural deformations underlying the non-linear evolution of the fluidic resistance of our foam with increasing compressive strain. The affine constriction of circular pores into ellipses, observed initially at small strains, eventually progresses into widespread collapse of cells at larger strains, accompanied by a rapid increase in resistance with applied force. A complete occlusion of internal flow paths occurs beyond a critical force approximately given by $F_C \sim 1/\eta$ = 50 N, corresponding to maximal compaction of cells across the full thickness of the sheet; Equation 9 correctly reflects this behavior in the limit $\xi(F \to 1/\eta) = \infty$.

As in the case of the foam-enabled DAC, our soft force-sensing resistors—packaged in the form factor of a pushbutton—may be integrated into pneumatic textile actuators, allowing analog control of the working pressure based on tactile inputs from the user. As an example, we show a textile bending actuator with an embedded force-sensing circuit (Figure 6d; Movie S3, Supporting Information), the curvature of which changes in response to force applied by the user on the pushbutton. Going beyond graded control of actuators, the capability to transduce force cues directly into fluidic signals suggests an array of exciting applications within the space of haptics and human communication.[41,42] For instance, deploying the force sensor as a fluidic transmitter, both analog and digital messages may be exchanged between human users entirely using pneumatic pressure signals (**Figure 7**a; Movie S4, Supporting Information). To this end, we set up a point-to-point communication link wherein force patterns keyed in by the sender are converted by the foam-enabled sensor (i.e., pushbutton) into pressure signals transmitted along a pneumatic "wire;" at the receiving end, a haptic sleeve worn on the upper arm converts the pressure signals back into squeeze cues that can be felt by the recipient. During tests with human users, both analog (multilevel) force patterns as well as digital (Morse-encoded) text messages—relayed via pneumatic signals generated by the pushbutton—were decoded and replicated by the recipient with perfect accuracy (Figure S11 and

S12, Supporting Information). Such pneumatic data links, devoid of electronic components, may be safely deployed to enable reliable and noise-free communication between users in industrial environments with high electromagnetic interference, or to secure operator-to-patient communication during diagnostic procedures such as magnetic resonance imaging (MRI). Even in electronically non-disruptive spaces, foam-enabled fluidic haptic systems could offer a potential means of conveying touch cues and gestures without direct physical contact between human users, such as across infection barriers to promote the comfort and psychological well-being of patients.[43]

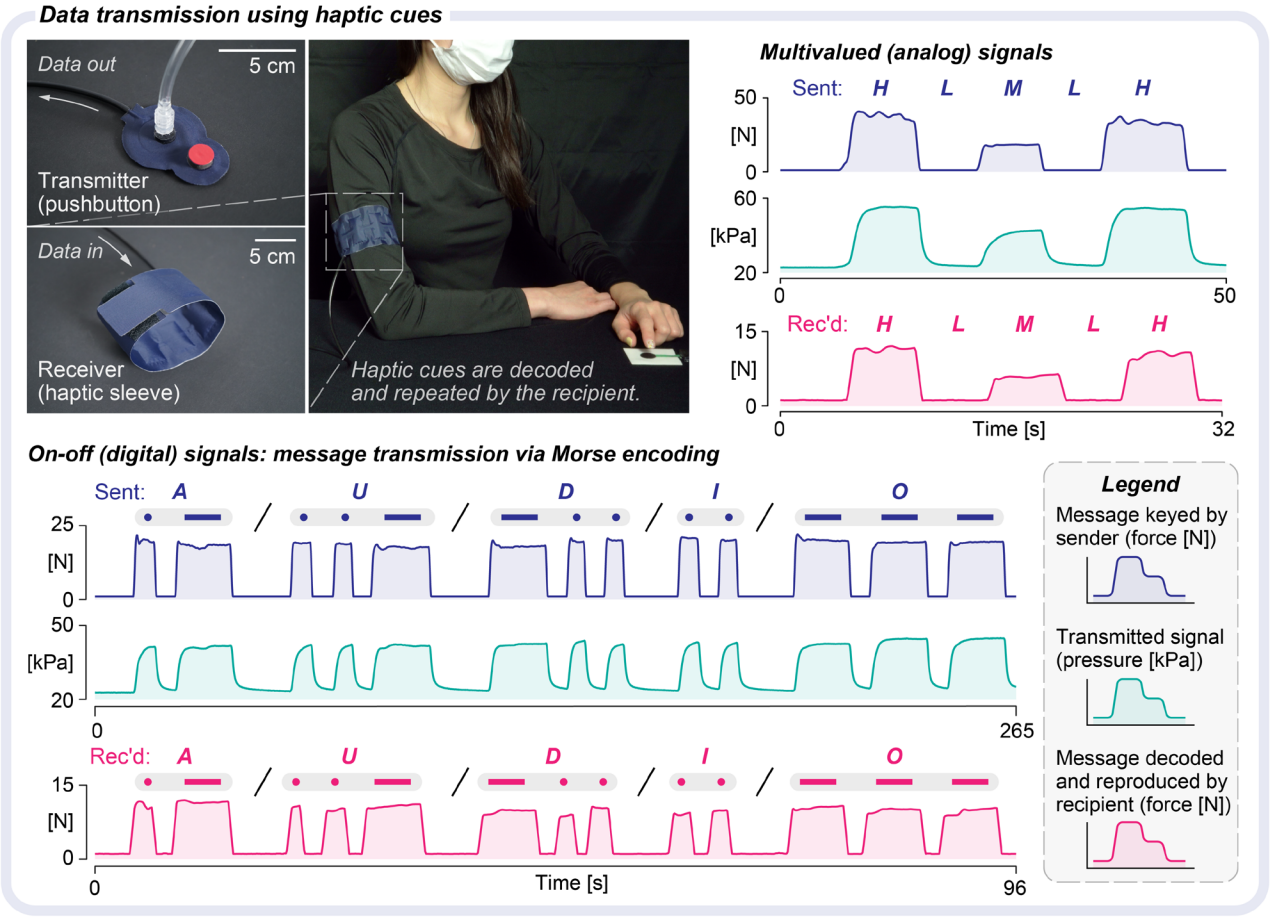

Figure 7. We combined a foam-enabled force sensor (the transmitter) and a wearable haptic sleeve (the receiver) to create a fluidic data transmission system for point-to-point communication between human users. The transmitter converts the force pattern keyed by the sender into pressure signals sent via the pneumatic link; at the other end, the receiver converts these signals back into force cues that can be felt by the recipient. Multiple data sequences, including both analog force patterns as well as digital (Morse-encoded) messages, transmitted by the sender were correctly decoded and reproduced by the recipient. (Also see Figure S11 and S12, Supporting Information.)

3. Discussion

Despite their passive mode of operation and simple transfer characteristics, accurately sized linear resistors are indispensable to the design and functionality of modern analog and digital systems.

Given the ubiquitous need for resistors and their versatile yet essential role in almost all sensing and control circuits, the development of new designs and embodiments that enhance the linearity, resilience, and manufacturability of resistors can yield substantial benefits through improved circuit reliability and lower costs. The availability of soft, compact, customizable, and mass-producible resistors is crucial to ensuring the viability of current and future generations of fluidic soft robots, and for enabling the miniaturization of logic and sensing circuitry required to build unencumbered wearables, untethered robots, and scalable robotic swarms.

Borrowing from the architecture of electronic integrated circuits, resistors in microfluidic chips have traditionally been realized as long and narrow fluidic channels, typically laid out in a serpentine pattern to achieve a compact footprint on the device. Despite the apparent simplicity of serpentine resistors, a direct translation of this conventional design from rigid or semi-rigid substrates (e.g., glass, plastics, and silicones) used in microfluidics to flexible sheet-based materials (such as fabrics) used in wearables, is beset by engineering and manufacturing hurdles. Unlike microfabrication techniques such as cleanroom photolithography, the resolution of geometric features attainable using stacked laminate assembly of textile sheets is usually limited to about 1 mm, enforcing a lower bound on the size of embedded fluidic pathways. Narrow channels require careful alignment of the masked textile layers during stacking, and are prone to blockages caused by the TPU flash produced during heat sealing; even when fabricated correctly, such channels readily kink under routine flexion and bending of wearable devices during use. Further complexities arise due to fluid-structure interactions in textile channels which inflate in response to gas pressure; these two-way interactions produce non-linear variations in cross section, both along the length of a channel as well as with changing flow conditions. The resistance of a flow channel is highly sensitive to its cross-sectional dimensions, as illustrated by the Hagen-Poiseuille equation which predicts a quartic dependence of the resistance on the radius for circular channels. Consequently, limitations in manufacturing tolerances together with pressure-dependent changes in cross-section pose significant difficulties in designing textile-embedded channels with linear, predictable, and reproducible flow characteristics.

Beyond the material- and process-related challenges specific to sheet-based devices, fundamental differences in flow dynamics accompany the change in working fluid from an incompressible viscous liquid (water) to a compressible and relatively inviscid gas (air). Unlike aqueous flows inside microfluidic channels that are dominated by viscous losses, air flow within millimetric textile channels is characterized by larger Reynolds numbers, with attendant flow effects such as inertial losses, turbulence, and flow choking. The stochastic nature of flow transitions, such as the onset of turbulence, renders the flow of gases through soft channels unpredictable and difficult to analyze,

and vitiates the linear response of channel-type resistors where such response may be desirable or even critical to the intended function of the fluidic circuit.

Exemplifying the advantages of our hybrid paradigm for circuit design, foam-enabled resistors circumvent these difficulties by shifting the locus of fluidic control away from artificial channels defined by engineered material boundaries, toward natural channels defined by the intrinsic structure of the porous material. The micrometric size of pathways within the foam sheet ensures that the gross flow remains dominated by viscous effects, yielding a linear response across a wide range of flow rates and upstream pressures. Besides enabling the construction of low-profile fluidic components, the confinement of the flow within two-dimensional sheets permits us to leverage the scale invariance of the flow field: insofar as the resistance is unchanged under isometric scaling, individual resistors may be scaled down to fit within the available device footprint, or scaled up to accommodate larger flow rates without incurring inertial non-linearities in the response curve.

Secondary benefits of our hybrid approach accrue from the careful selection of fluidic materials: The durability of open-cell foam and its resilience under repeated compression render it an excellent structural material for soft devices. As demonstrated in this work, polyurethane sheet resistors adhere directly to the TPU coating on heat-sealable fabrics, allowing facile embedment of fluidic components during stacked laminate assembly of textile layers. When used as pull-down devices, foam-enabled resistors naturally double up as acoustic mufflers by dampening the noise of the exhaust stream, akin to porous silencers used in industrial pneumatic systems. They thus allow quieter operation of pneumatic logic circuits in wearable robots and assistive devices, enhancing user comfort and experience.

The switch to foam-enabled circuit components is not entirely without disadvantages, one of which is the material preparation (nylon cladding) required prior to fabrication. Combining multiple soft materials—such as textiles and foam—is often inevitable in soft robotics, but nevertheless represents a departure from the ideal of a monolithic, jointless construction wherein both fluidic and structural elements are realized using a single soft material to achieve seamless integration of form and function. In a composite assembly, differences in mechanical properties between soft materials can create structural weak points susceptible to failure. As a case in point, the adhesion between foam sheets and textile layers is weaker than a direct textile-to-textile bond, because of which foam-fabric interfaces represent the primary failure points limiting the pressure rating of heat-sealed pneumatic devices. Future iterations of our devices will thus seek to mitigate the shortcomings of our current approach through exploration of better materials and manufacturing processes. Finally, the effect of out-of-plane bending on the resistance of foam sheets also warrants a more in-depth investigation,

although preliminary experience with our textile devices indicates that this effect is secondary to that of transverse compression.

In conclusion, foam-enabled fluidic devices represent a promising step toward hybrid robotic architectures that will fully leverage the sensing and computing capabilities of soft materials, thereby synergizing the advantages of circuit-based and material-based approaches to intelligence. With sustained innovations in materials and manufacturing methods, we are optimistic that such hybrid systems will in the future enable the emergence of a new class of reliable, efficient, and streamlined wearables and robots made from soft fluidic circuit materials.

4. Experimental Section

Fabrication of resistors: We built our resistors using flexible sheets of open-cell polyurethane foam (PORON ShockSeal, Rogers Corp.) with a density of 320 kg m^{-3}, tensile strength of 689 kPa, tear strength of 1.8 kN m^{-1}, and a compression force deflection rating of 110 kPa at 25% deflection. To ensure in-plane confinement of the flow, two layers of thermoplastic nylon (Stretchlon 800, Airtech International Inc.), each 50 μm thick and of areal density 1.11 g cm^{-2}, were heat sealed to the top and bottom faces of the foam sheet at 220 °C under pressure (Figure 2a) using a benchtop heat press (DK20SP, Geo Knight & Co Inc.). We confirmed through scanning electron microscopy (SEM) that thermal reflow of the nylon during the heat-sealing process created well-adhered and gas-impermeable layers encasing the foam sheet, sealing off open pores on the sheet faces (Figure S4, Supporting Information). Finally, annular resistors of the required radial dimensions were hand-cut from the heat-sealed sheets with the aid of hollow gasket punches (66004, Mayhew Steel Products Inc.).

To create composite resistors, nylon-sealed foam sheets were stacked with an interlayer of adhesive TPU (Iron-on fusible interfacing, Outus) and thermally bonded at 180 °C under pressure (Figure 2d). The same technique was employed to stack annular resistors to create the force-sensing pushbuttons shown in Figure 6 and 7. Where required, open ends of the resistors were sealed off using disks of nylon taffeta fabric, affixed to the top or bottom faces using heat-activated TPU adhesive.

Microscopic imaging: Images were recorded using a Quanta FEG 400 (FEI Co.) scanning electron microscope (secondary electron detector, 10 kV accelerating voltage) at the Shared Equipment Authority at Rice University. As foam is electrically non-conductive, a 10 nm layer of gold was sputtered onto the sectioned samples to deter charge accumulation and enhance image quality. To create the sequence in Figure 6c, we compressed 2.38 mm (3/32") thick specimens of heat-sealed foam in a stage-mountable micro-vise (15340, Ted Pella Inc.), trimmed the sample edges flush with

the vise jaws, and sputtered a 20 nm layer of gold onto the sectioned face prior to imaging.

Four-point measurement of sheet resistance: To create the fluidic ports, four holes (each of radius a = 1.5 mm and spaced s = 15 mm apart) were punched in the middle of a square sheet resistor (of side length L = 28 cm) along the centerline (Figure 2b). Luer lock connectors were glued to the ports using epoxy adhesive to enable quick and leakproof coupling with pneumatic lines. Pressure and flow rate measurements were made using electronic pressure sensors (ADP5151, Panasonic Corporation) and a Pelton turbine flow meter (FLR1000 series, Omega Engineering Inc.) respectively, all connected to a computer-based data acquisition device (USB-6210, National Instruments). Readings from the flowmeter were suitably corrected for gas density variations as recommended by the manufacturer for measurements on air above atmospheric pressure. To minimize experimental errors, we automated the test protocol as well as the data acquisition, processing, and fitting routines using custom MATLAB scripts (MathWorks Inc.); automatic regulation of the air flow rate from the software was enabled by a proportional solenoid valve (EV-P-10-25-A0-V, Clippard) placed upstream of the inlet port, and controlled via the data acquisition system.

Measurement of fluidic resistance: Measurements of the fluidic resistance of individual annular resistors were performed using the same automated system used for four-point measurements on sheet resistors. The resistance was extracted using a two-parameter (slope and intercept) linear fit to the pressure drop vs flow rate curve, to mitigate errors arising from zero drift of the inlet pressure sensor. Typically, replicate flow curves were obtained for two or three different resistors of identical dimensions, and their slopes averaged to generate the data shown in Figure 3; error bars in these plots denote the range of measured resistances across all replicates.

Characterization of inverter output pressure: For measurements of output pressure and signal propagation delay, we built a set of three modular textile inverters with Luer lock couplings on the output line, allowing us to "hot swap" (i.e., switch out) pull-down resistors of various sizes during experiments. Compressed air for operating the inverter was sourced at 50 kPa from the building air supply through a diaphragm-type pressure regulating valve (PR364, Parker Hannifin Corp.); the fluidic resistance of the supply manifold was simulated by inserting a 95-cm long section of 1.67-mm diameter polyethylene tubing between the pressure regulator and the supply port of the inverter. With the input signal to the inverter tied low (i.e., held at atmosphere pressure), we used digital pressure gauges (MG1-30-A-9V-R, SSI Technologies Inc.) to record both the supply (gauge) pressure p_S upstream of the tube and the output (gauge) pressure p_O of the inverter in the logical high state. Three such replicate measurements were averaged to obtain each value of p_O/p_S shown in

Figure 4b.

Measurement of signal propagation delay: We connected three textile inverters in series to simulate a multistage digital logic circuit (Figure 4c); a low-frequency square wave input was provided to the first inverter in the chain by means of a manually operated toggle valve connected to a 50 kPa pressure source. Electronic pressure sensors (ADP5151, Panasonic Corporation) connected to a computer-based data acquisition device (USB-6210, National Instruments) were used to record transient pressure traces of the input signal $p_0(t)$ and the output signal $p_3(t)$ of the three-stage network. The recorded data was then analyzed to determine the cumulative delay (= $3\Delta t$) between corresponding transitions (rising or falling edges) of the input signal and output signals; a rising or falling edge was identified as the instant when the signal (gauge) pressure $p(t)$ crossed above or below 50 % of the supply (gauge) pressure p_S. Each data point in Figure 4d was obtained by averaging the individual time delays measured for four successive transitions (two rising and two falling edges) of the input signal.

Fabrication of textile devices: The linear and bending actuators, 2-bit DACs, force sensors, and the haptic sleeve were made from heat-sealable textiles using a bespoke paper-masking technique developed in our prior work.[14] Briefly, we applied an adhesive paper tape (V0821, Vinyl Ease) to the TPU-coated side of heat-sealable nylon taffeta fabric (70 denier; Seattle Fabrics); we then patterned the taped fabric using a desktop cutting plotter (Cricut Maker, Cricut Inc.) to create individual textile layers containing masked regions that will form the requisite channels, pouches, or other internal fluidic spaces after stacked laminate assembly in a heat press (Figure S8–10, Supporting Information). The masked layers were carefully aligned and sealed together using a benchtop press (DK20SP, Geo Knight & Co Inc.) heated to 200 °C. Embedded resistors, if any, were positioned directly between the facing textile sheets at the required locations prior to heat sealing; these resistors were secured in place within the finished device by direct adhesion with the TPU-coated textile. Finally, fluidic ports were attached to the inlet and outlet channels of the device using two-part epoxy adhesive to create airtight joints.

The textile bending actuators in Figure 5e and 6d consisted of ten fluidically connected pouch motors (each of size 16 mm by 40 mm), overlaid on a 5-mm wide support bladder that extended over the full length (200 mm) of the device. During operation, the bending moment exerted by the pouch motors is resisted by the stiffness of the inflated support bladder, which was maintained at a constant internal pressure of p_B = 100 kPa. To build the textile linear actuator shown in Figure 5f, we created an array of eight serially linked large-contraction pouch motors (of dimensions 56 mm by 30 mm by 20 mm), based on a gusseted pouch design reported in a previous study.[44] The restoring force

resisting the contraction of the motors was provided by two 1.13-kg (2.5-lb) barbell plates suspended from the bottom of the actuator. The haptic sleeve in Figure 7a was designed with six circumferentially arrayed pouches, each of size 40 mm by 20 mm, which on pressurization generates an radially inward squeeze force; the mechanical response of a similar haptic squeeze band was characterized in detail in prior work.[45] The sleeve was equipped with matched hook and loop fasteners at the two ends to secure the device around the user's arm.

Pressure and flow rate modulation using the textile DAC: Digital pressure signals to the 2-bit DAC were provided from a pair of manually operated, self-exhausting toggle valves connected to an air manifold at supply pressure. The pressure and flow outputs from the DAC for different binary inputs were measured using a digital pressure gauge (MG1-30-A-9V-R, SSI Technologies Inc.) and a turbine flow meter (FLR1006D, Omega Engineering Inc.), respectively.

To demonstrate the regulation of flow rate using binary inputs, we employed a 16-gauge blunt-tip needle (of length 56.7 mm and inner diameter 1.346 mm) as a nozzle to collimate the output flow from the low-resistance DAC (d = 2.38 mm) into a free jet exiting into quiescent air. In the experiment shown in Figure 5c, the jet was positioned to impinge on a circular Joule heater (Omegalux KHR-3/10, Omega Engineering Inc.) placed 10 cm away from the nozzle exit. The heater had a room-temperature resistance of 198 Ω and a circular active region approximately 70 mm in diameter, and was energized by a constant current of 0.25 A provided from a DC power supply (RD6018, Riden). A T-type thermocouple probe taped to the heater surface and connected to a handheld digital thermometer (51 II, Fluke Corp.) enabled us to record the steady state temperatures at the center of the heater for various binary inputs to the DAC. For the experiment in Figure 5d, the jet was aimed toward the lighted wicks of an array of wax candles placed at increasing distances from the nozzle.

For pressure regulation experiments shown in Figures 5e–g, we employed fiducial markers (red beads in Figure 5e and the yellow dot in Figure 5g) to track the motion of textile actuators using video recordings and still photographs taken during the experiment. The radius of curvature of the bending actuator was extracted by fitting a circle through the red markers positioned along its length. The contraction of the linear actuator was inferred from the vertical displacement of the yellow marker affixed to its bottom end.

Measuring resistance change under compression: For designating the size of annular resistors used in our force-sensing circuits, we adopt the 3-tuple shorthand $\langle r_1,\ r_2,\ d\rangle$, where the numbers r_1, r_2, and d respectively denote the inner radius, the outer radius, and the sheet thickness expressed in

millimeters. To build the fluidic voltage divider shown in Figure 6a, we used three identical $\langle 2, 15, 1.59 \rangle$ resistors, with one serving as the reference resistor and the other two forming the force-sensing stack; the output pressure p_O of the circuit was measured using a digital pressure gauge. For the pushbutton integrated with the textile bending actuator (Figure 6d), we used a $\langle 1.5, 15, 1.59 \rangle$ resistor as the reference and three $\langle 2, 7, 2.38 \rangle$ resistors to build the force-sensing stack. In both cases, the force exerted by the piston or by the user's finger was monitored by means of an electronic force-sensing resistor (FSR 402, Interlink Electronics Inc.) placed in line with the stack; its resistance was measured using a digital multimeter (26 III, Fluke Corp.), from which the applied force was inferred based on the sensor's calibration curve.

Data transmission using haptic cues: To create the fluidic point-to-point communication system, we leveraged the analog pressure output produced by our force sensor (the transmitter) to actuate haptic elements on a wearable pneumatic sleeve (the receiver), generating squeeze cues that can be perceived by a human recipient. Fluidic signals from the transmitter were conveyed to the receiver via a long flexible pneumatic tube. The strength of the force cues produced by the sleeve is largely determined by the supply pressure fed to the force sensor, which may be adjusted based on user preference and comfort; in our case, the peak operating pressure was set at approximately 50 kPa. The recipient was seated at a distance and facing away from the sender to prevent inadvertent visual or auditory feedback of the keyed message. We tested the performance of the system by transmitting both analog (multilevel) force patterns as well as digital (Morse-encoded) text messages; in each case, an initial training sequence (force pattern or five letter word) was first transmitted to acquaint the recipient with the sensation of haptic cues generated by the sleeve. This was followed by four distinct test sequences, all previously unknown to the recipient; after each sequence was fully transmitted, the recipient was asked to replicate the force pattern as discerned by them by tapping on an electronic force sensor. The sequences keyed in by the sender, and the corresponding reproductions by the recipient, are shown in Figure S11 and S12 (Supporting Information); despite small errors in replicating the two training sequences, all eight test sequences were decoded by the recipient with perfect accuracy.

Supporting Information

Supporting Information is available from the Wiley Online Library or from the author.

Acknowledgements

A.R. and T.F.Y. thank Te Anne Yap for assistance during experiments shown in Figure 6a. A.R. acknowledges support from the Rice University Academy of Fellows. R.M.R acknowledges support

from the U.S. Department of Energy (DOE) Innovation in Buildings (IBUILD) fellowship under DOE contract number DE-SC0014664. Scanning electron microscopy was performed using resources provided by the Shared Equipment Authority at Rice University. This material is based upon work supported by the National Science Foundation under grant no. CMMI-2144809.

Received: (will be filled in by the editorial staff)

Revised: (will be filled in by the editorial staff)

Published online: (will be filled in by the editorial staff)

References

[1] M. Wehner, R. L. Truby, D. J. Fitzgerald, B. Mosadegh, G. M. Whitesides, J. A. Lewis, R. J. Wood, *Nature* **2016**, *536*, 451.

[2] D. Rus, M. T. Tolley, *Nature* **2015**, *521*, 467.

[3] J. Shintake, V. Cacucciolo, D. Floreano, H. Shea, *Advanced Materials* **2018**, *30*, 1707035.

[4] C. Majidi, *Advanced Materials Technologies* **2019**, *4*, 1800477.

[5] A. Rajappan, B. Jumet, D. J. Preston, *Science Robotics* **2021**, *6*, 1.

[6] K. Becker, C. Teeple, N. Charles, Y. Jung, D. Baum, J. C. Weaver, L. Mahadevan, R. Wood, *Proceedings of the National Academy of Sciences* **2022**, *119*, e2209819119.

[7] B. Gorissen, D. Reynaerts, S. Konishi, K. Yoshida, J.-W. Kim, M. De Volder, *Advanced Materials* **2017**, *29*, 1604977.

[8] K. McDonald, T. Ranzani, *Frontiers in Robotics and AI* **2021**, *8*, 1.

[9] B. Jumet, M. D. Bell, V. Sanchez, D. J. Preston, *Advanced Intelligent Systems* **2022**, *4*, 2100163.

[10] P. Rothemund, A. Ainla, L. Belding, D. J. Preston, S. Kurihara, Z. Suo, G. M. Whitesides, *Science Robotics* **2018**, *3*, eaar7986.

[11] D. J. Preston, P. Rothemund, H. J. Jiang, M. P. Nemitz, J. Rawson, Z. Suo, G. M. Whitesides, *Proceedings of the National Academy of Sciences* **2019**, *116*, 7750.

[12] D. J. Preston, H. J. Jiang, V. Sanchez, P. Rothemund, J. Rawson, M. P. Nemitz, W. Lee, Z. Suo, C. J. Walsh, G. M. Whitesides, *Science Robotics* **2019**, *4*, eaaw5496.

[13] D. Drotman, S. Jadhav, D. Sharp, C. Chan, M. T. Tolley, *Science Robotics* **2021**.

[14] A. Rajappan, B. Jumet, R. A. Shveda, C. J. Decker, Z. Liu, T. F. Yap, V. Sanchez, D. J. Preston, *Proceedings of the National Academy of Sciences* **2022**, *119*, e2202118119.

[15] C. J. Decker, H. J. Jiang, M. P. Nemitz, S. E. Root, A. Rajappan, J. T. Alvarez, J. Tracz, L. Wille, D. J. Preston, G. M. Whitesides, *Proceedings of the National Academy of Sciences* **2022**, *119*, e2205922119.

[16] L. C. van Laake, J. de Vries, S. M. Kani, J. T. B. Overvelde, *Matter* **2022**, *5*, 2898.

[17] R. Z. Gao, C. L. Ren, *Biomicrofluidics* **2021**, *15*, 011302.

[18] M. Pishvar, R. L. Harne, *Advanced Science* **2020**, *7*, 2001384.

[19] H. Yasuda, P. R. Buskohl, A. Gillman, T. D. Murphey, S. Stepney, R. A. Vaia, J. R. Raney, *Nature* **2021**, *598*, 39.

[20] R. L. Truby, *Accounts of Materials Research* **2021**, *2*, 854.

[21] R. L. Truby, L. Chin, A. Zhang, D. Rus, *Science Advances* **2022**, *8*, eabq4385.

[22] A. L. Evenchik, A. Q. Kane, E. Oh, R. L. Truby, *Annual Review of Materials Research* **2023**, *53*, 225.

[23] C. El Helou, P. R. Buskohl, C. E. Tabor, R. L. Harne, *Nat Commun* **2021**, *12*, 1633.

[24] C. El Helou, B. Grossmann, C. E. Tabor, P. R. Buskohl, R. L. Harne, *Nature* **2022**, *608*, 699.

[25] H. Lu, M. Zhang, Y. Yang, Q. Huang, T. Fukuda, Z. Wang, Y. Shen, *Nat Commun* **2018**, *9*, 3944.

[26] A. Pal, M. Sitti, *Proceedings of the National Academy of Sciences* **2023**, *120*, e2212489120.

[27] S. Joe, O. Bliah, S. Magdassi, L. Beccai, *Advanced Science* **2023**, 2302080.

[28] T. Chen, M. Pauly, P. M. Reis, *Nature* **2021**, *589*, 386.

[29] A. Pal, V. Restrepo, D. Goswami, R. V. Martinez, *Advanced Materials* **2021**, *33*, 2006939.

[30] L. J. Kwakernaak, M. van Hecke, *Phys. Rev. Lett.* **2023**, *130*, 268204.

[31] B. Van Raemdonck, E. Milana, M. De Volder, D. Reynaerts, B. Gorissen, *Advanced Materials* **2023**, 2301487.

[32] L. Wu, D. Pasini, *Advanced Materials* **2023**, *35*, 2301109.

[33] G. K. Batchelor, *An Introduction to Fluid Dynamics*, Cambridge University Press, Cambridge, **2000**.

[34] A. Uhlir, *The Bell System Technical Journal* **1955**, *34*, 105.

[35] F. M. Smits, *The Bell System Technical Journal* **1958**, *37*, 711.

[36] M. M. Mano, *Digital Logic and Computer Design*, Prentice-Hall International, London, **1979**.

[37] P. Horowitz, W. Hill, *The Art of Electronics*, Cambridge University Press, New York, **2021**.

[38] F. P. Incropera, D. P. DeWitt, T. L. Bergman, A. S. Lavine, *Fundamentals of Heat and Mass Transfer*, John Wiley & Sons, Hoboken, NJ, **2007**.

[39] A. N. Gent, K. C. Rusch, *Journal of Cellular Plastics* **1966**, *2*, 46.

[40] M. A. Dawson, J. T. Germaine, L. J. Gibson, *International Journal of Solids and Structures* **2007**, *44*, 5133.

[41] J. Yin, R. Hinchet, H. Shea, C. Majidi, *Advanced Functional Materials* **2021**, *31*, 2007428.

[42] B. Jumet, Z. A. Zook, A. Yousaf, A. Rajappan, D. Xu, T. F. Yap, N. Fino, Z. Liu, M. K.

O'Malley, D. J. Preston, *Device* **2023**, 100059.

[43] D. Li, J. Zhou, K. Yao, S. Liu, J. He, J. Su, Q. Qu, Y. Gao, Z. Song, C. Yiu, C. Sha, Z. Sun, B. Zhang, J. Li, L. Huang, C. Xu, T. H. Wong, X. Huang, J. Li, R. Ye, L. Wei, Z. Zhang, X. Guo, Y. Dai, Z. Xie, X. Yu, *Science Advances* **2022**, *8*, eade2450.

[44] J. H. Jang, B. Jamil, Y. Moon, A. Coutinho, G. Park, H. Rodrigue, *IEEE/ASME Transactions on Mechatronics* **2023**, 1.

[45] B. Jumet, Z. A. Zook, D. Xu, N. Fino, A. Rajappan, M. W. Schara, J. Berning, N. Escobar, M. K. O'Malley, D. J. Preston, in *2022 IEEE 5th International Conference on Soft Robotics (RoboSoft)*, **2022**, pp. 741–746.